



Cite this: *Phys. Chem. Chem. Phys.*,
2025, 27, 14432

Spin–orbit coupling effects hidden behind the photophysics of phosphorescent chiral cyclometalated Pt(II) complexes[†]

Thomas Groizard, Souvik Mandal, Christophe Gourlaouen [‡] and Chantal Daniel *

The electronic and (chiro-) optical properties of $[\text{Pt}(\text{pCpy})(\text{acac})]$ **1** and $[\text{Pt}(\text{pCpz})(\text{acac})]$ **2** (pCpy = 2-[2,2]-paracyclophane-4-yl)pyridyl; pCpz = 1-[2,2]-paracyclophane-4-yl)pyrazolyl; acac = dimethyl-substituted acetylacetone), representative of phosphorescent chiral cyclometalated Pt(II) complexes, are investigated by means of density functional theory (DFT) and its time-dependent extension so-called TD-DFT, including spin–orbit coupling (SOC) effects. The computed absorption, phosphorescence and circularly polarized luminescence (CPL) spectra are compared to the available experimental spectra, and analysed on the basis of spin–orbit interactions and electronic excited state sub-levels. The major role of the SOC is established and deciphered for both complexes. Spin–orbit sub-levels of the low-lying triplet manifold not only perturb the absorption spectra by a 60–70 nm shift to the red, but entirely control the phosphorescence and CPL activities, in terms of intensity and composition. It is shown that the substitution of a pyridyl ligand in **1** with a pyrazolyl in **2** has dramatic consequences on the photophysics of these “case-study” molecules. Indeed, the character and the energetics of the lowest triplet states participating in the emission properties are drastically affected by this change of ligands. Whereas $[\text{Pt}(\text{pCpy})(\text{acac})]$ **1** can be considered as an “easy case”, both experimentally and theoretically, $[\text{Pt}(\text{pCpz})(\text{acac})]$ **2** represents a challenge computationally due to the presence of two nearly degenerate emissive triplet states. The correlation between the structural/electronic properties of the excited states contributing to the spectra is discussed as well as the early time (<1 ps) photophysics simulated by non-adiabatic quantum dynamics for the two complexes.

Received 15th April 2025,
Accepted 7th June 2025

DOI: 10.1039/d5cp01450f

rsc.li/pccp

1 Introduction

Over the last three decades,¹ a multitude of third-row transition metal complexes (TMCs) with a variety of ligands have been synthesized to optimize the luminescent properties and to control the branching ratio between radiative and non-radiative decays.^{2–6} The energy gap between the lowest triplet metal-centered (MC) and metal-to-ligand-charge-transfer (MLCT) or ligand-centered (LC) excited states and their coupling with the electronic ground state and with the environment were mainly considered. Further analysis scrutinized spin–orbit coupling (SOC) effects which are responsible for efficient intersystem

crossing (ISC) and subsequent population of the lowest potentially luminescent triplet excited state, ³LC possibly contaminated by ³MLCT state contribution. The introduction of multidentate ligands, containing metal–carbon bonds *via* pincer cyclometalated substitution, initiated applications in functional materials, chromic devices, memory storage, supramolecular assemblies and probes or ion sensors.^{7–12} Most of the TMCs, used in organic light-emitting devices (OLEDs), for instance, are either achiral or racemic mixtures.¹³ However, enantiopure compounds might provide circularly polarized luminescence (CPL) emission opening opportunities to overcome technical issues as well as emerging applications. CPL materials may contribute to the reduction of power consumption in light-emitting devices¹⁴ and are of central importance in applications such as three-dimensional OLED devices, quantum computing,¹⁵ spintronics,¹⁶ and bio-imaging.

The development of chiral TMCs has been mainly driven by their application in asymmetric catalysis, near infra-red (NIR) chiroptics, structural probe ferroelectricity, and stereochemistry with a few studies dedicated to their CPL activity as illustrated by early experiments reported for Ir(III) complexes.^{17,18} Despite

Laboratoire de Chimie Quantique Université de Strasbourg CNRS UMR7177,
Institut Le Bel 4 Rue Blaise Pascal, 67000 Strasbourg, France.

E-mail: c.daniel@unistra.fr

† Electronic supplementary information (ESI) available. See DOI: <https://doi.org/10.1039/d5cp01450f>

‡ Present address: Laboratoire de Modélisation et Simulations Moléculaires, Université de Strasbourg CNRS UMR 7140 Chimie de la Matière Complexe 4 Rue Blaise Pascal, 67000 Strasbourg, France. E-mail: gourlaouen@unistra.fr



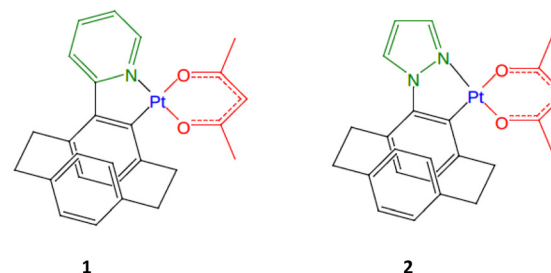
excellent photophysical properties these molecules exhibit a quite low electro-luminescence dissymmetry factor. Introduction of ligand-based helicoidal chirality, as proposed in metall-helicene Ir(III), Pt(II) and Re(I) complexes,^{19–25} allowed the tuning of both electric and magnetic transition dipole moments keeping high electro-luminescence (EL) efficiency together with significant chiro-optical activity. However, an in-depth fundamental understanding of the parameters governing chirooptical properties in these phosphorescent TMCs and a full rationalization of such parameters is still lacking for optimizing the design of new CPL emitters.

Whereas the S_n , $T_n \rightarrow S_0$ luminescent properties can be determined easily on the basis of the low-lying excited state structural properties,²⁶ a more challenging step forward is the modeling of the electronic circular dichroism (ECD) and CPL spectra. Indeed, computational protocols have been mainly developed for organic molecules, the circularly polarized light responses of which are governed by S_0 and a few low-lying singlet states.²⁷ The spin-allowed ECD and CPL spectra are computed from the oscillatory and rotational strengths associated with the active singlet excited state at the Franck–Condon (FC) geometry.

Taking into account the SOC effects in the computation of ECD and CPL spectra needs another strategy. Indeed, calculating these properties at the triplet excited state equilibrium geometry, within a relativistic perturbative approach,²⁸ leads to allowed electric and magnetic dipole transitions based on spin-orbit perturbed ground and excited states. Both oscillator and rotational strengths associated with “spin-orbit” transitions become accessible.

On the basis of a new computational protocol developed in ORCA²⁹ to interpret and predict photophysical properties in a series of chiral non-helicenic and helicenic Re(I) complexes, extensively investigated experimentally by Crassous *et al.*,^{21,22} we have established the factors that control the phosphorescence, the radiative and non-radiative decays and the CPL activity of these molecules.³⁰ We have shown that the electronic character of the low-lying singlet and triplet excited states and their spin-orbit splitting and mixing play a major role in the control of the zero-field splitting (ZFS) parameters and of the magnetic and electric transition dipole moment relative orientations. Both the ligand localized nature of the emissive state and the steric effects induced by helicenes influence drastically the phosphorescence relaxation time and the CPL intensity. Extending the structural diversity by introducing planar chirality directly coordinated onto a metal center may lead to a specific response of the complexes in terms of CPL activity because of the presence of low-lying charge transfer (CT) states. This could help in a deeper understanding of the influence of electronic and structural parameters on the CPL activities in chiral emitters. It would also be of interest to use ligands made *via* more straightforward synthetic protocols.

The use of paracyclophane derivatives as chiral auxiliary ligands has offered a platform for a number of new organic compounds^{31–33} as well as transition metal complexes.^{34,35} Combining photophysical and optoelectronic properties with chirality in potentially phosphorescent Pt(II) and Ir(III) complexes,



Scheme 1 Schematic structures of $[\text{Pt}(\text{pCpy})(\text{acac})]$ **1** and $[\text{Pt}(\text{pCpz})(\text{acac})]$ **2**.

Thompson *et al.*³⁵ have shown that whereas a substitution by monoanionic cyclophane ligand 2-(2,2-paracyclophane-4-yl)-pyridyl (pCpy) leads to highly emissive molecules at room temperature, pyrazolyl analogs, 1-(2,2-paracyclophane-4-yl)-pyrazolyl (pCpz), provide weakly emissive compounds. This has been attributed to thermally activated non-radiative decay from high-lying triplet states in the pyrazolyl complex. However, the potential for chiro-optical activity has not yet been experimentally investigated.

Herein, we propose a detailed theoretical investigation of the photophysics and (chiro-) optical properties of $[\text{Pt}(\text{pCpy})(\text{acac})]$ **1** and $[\text{Pt}(\text{pCpz})(\text{acac})]$ **2** (Scheme 1), synthesized by Thompson *et al.*³⁵ Our objective is to analyze and understand the different luminescence behavior observed experimentally and to predict the opto-chiral activity in this class of emitters on the basis of spin-orbit interactions, structural and electronic properties. It will be shown that despite their apparent similarity the two molecules are very different in terms of potentially emissive states and spin-orbit interactions. In addition, whereas Pt-Cpy **1** is an “easy case” with one single emissive T_1 electronic state, Pt-Cpz **2** is a “tough case”, challenging for both experimentalists and theoreticians, with potential emission governed by two nearly-degenerate triplet excited states.

2 Theoretical background

2.1 Methodological approach

The theory underlying the computational protocol developed in ORCA for calculating absorption, spontaneous luminescence, ECD and CPL cross sections as well as their respective radiative rates is detailed in our seminal article dedicated to the Re(I) complexes.³⁰ The cross sections are expressed at the first-order perturbative treatment within the weak field approximation and the general expression of Fermi's golden rule, whereas the radiative rates are calculated within the electric dipole approximation.

The cross sections are given by

$$\sigma_{\text{ABS/PL}}(\omega) = \frac{4\pi^2}{c(\omega_{\text{ABS/PL}} - \omega_{\text{FI}})} |T_{\text{IF}}|^2 \delta(E_{\text{FI}} \pm \omega_{\text{ABS/PL}}) \quad (1)$$

where $\omega_{\text{ABS/PL}}$ are the excitation and emission photon energies, respectively, while ω_{FI} is the energy difference between the initial and final states reached in the absorption or the photoluminescence processes. $T_{\text{IF}} \sum_{j=1}^N \langle \text{I} | e^{ikr_j} (\varepsilon \cdot \hat{p}_j) | \text{F} \rangle$ denotes the

transition probability employing the full field-matter interaction operator (FFMIO), r_j and \hat{p}_j are the position and the momentum operators of the j^{th} particle, k and ε denote the wave and polarization vectors of the incident radiation field. E_{FI} is the transition energy, δ refers to the line-broadening arising from the lifetimes of the relevant final states, and c is the speed of light.

Within the electric dipole approximation (ED) the respective radiative rates for the absorption and the spontaneous photoluminescence are given by eqn (2) and (3), respectively:

$$k_{\text{ABS}}(\omega) = \frac{4\pi^2\omega_{\text{ABS}}}{3} \sum_{\text{F}} |\langle \Psi_1 | \hat{\mu} | \Psi_{\text{F}} \rangle|^2 \delta(E_{\text{FI}} \pm \omega_{\text{ABS}}) \quad (2)$$

$$k_{\text{PL}}(\omega) = \frac{4\omega_{\text{PL}}^3 n^2}{3\hbar c^3} \sum_{\text{F}} |\langle \Psi_1 | \hat{\mu} | \Psi_{\text{F}} \rangle|^2 \delta(E_{\text{FI}} \pm \omega_{\text{PL}}) \quad (3)$$

where $\hat{\mu}$ defines the electric dipole operator as $\hat{\mu} = \sum_A Z_A \hat{R}_A - \sum_i \hat{r}_i$, here A sums over nuclei with charges Z_A at positions R_A , i over the electrons, n is the refractive index, and \hbar is the Planck constant divided by 2π .

The formalism, inspired by the one developed for magnetic circular dichroism (MCD),³⁶ allowed the proposal of a unified framework for the calculation of both the optical (absorption/emission) and chiro-optical (ECD/CPL) intensities and radiative rates. Details about the formulation of the MCD expressions within the framework of the full field-matter interaction operator (FFMIO) can be found in the ESI.[†]

By analogy, within the ED approximation, the equations developed for MCD can be used to generate absorption and luminescence cross sections. Including electric (ED) and magnetic dipole (MD) interactions upon orientational averaging will generate the respective ECD and CPL radiative transition rates:

$$k_{\text{ECD}}(\omega) = \frac{16\pi^2\omega_{\text{ECD}}}{3} \sum_{\text{F}} \text{Im}(|\langle \Psi_1 | \hat{\mu} | \Psi_{\text{F}} \rangle \cdot \langle \Psi_{\text{F}} | \hat{m} | \Psi_1 \rangle|) \delta(E_{\text{FI}} \pm \omega_{\text{ECD}}) \quad (4)$$

$$k_{\text{CPL}}(\omega) = \frac{16\omega_{\text{CPL}}^3 n^2}{3\hbar c^3} \sum_{\text{F}} \text{Im}(|\langle \Psi_1 | \hat{\mu} | \Psi_{\text{F}} \rangle \cdot \langle \Psi_{\text{F}} | \hat{m} | \Psi_1 \rangle|) \delta(E_{\text{FI}} \pm \omega_{\text{CPL}}) \quad (5)$$

In the above expressions, $\hat{\mu}$ defines the electric dipole operator while \hat{m} is the respective magnetic dipole operator $\hat{m} = \frac{1}{2m_e c} \sum_i r_i \times \hat{p}_i$, m_e is the electron mass and $\text{Im}(|\langle \Psi_1 | \hat{\mu} | \Psi_{\text{F}} \rangle \langle \Psi_{\text{F}} | \hat{m} | \Psi_1 \rangle|)$ represents the rotatory strength (R_{IF}).

The ECD and CPL spectral intensities are represented against normalized absorption and photoluminescent intensities defining, similar expressions for, the respective dissymmetry factors g_{abs} and g_{lum}

$$g_{\text{abs}}(\text{ECD}) \text{ or } g_{\text{lum}}(\text{CPL}) = 2 \frac{I_{\text{LCP}} - I_{\text{RCP}}}{I_{\text{LCP}} + I_{\text{RCP}}} \sim \frac{4R}{D}, \quad (6)$$

$-2 < g_{\text{abs}} \text{ or } g_{\text{lum}} < 2$

where $I_{\text{LCP/RCP}}$ is the left and right polarized components of the involved absorption or emission process. D and R are the

squares of the transition electric dipole and the rotatory strength, respectively. Expression (6) approximation is applicable for both organic or organometallic systems with negligible magnetic dipole contribution and comes from the following equation:

$$g_{\text{lum}} = \frac{c|\mu| \cdot |m| \cos \theta}{c^2|\mu|^2 + |m|^2} \quad (7)$$

where c is the speed of light, μ is the electric transition dipole associated with the emissive state, m is the magnetic transition electric dipole moment and θ is the angle between both transition dipole moments.

Spin-orbit coupling (SOC) along with the Zeeman interactions introduced in the framework of quasi-degenerate perturbation theory (QDPT)³⁷ act as a perturbation to the non-relativistic Hamiltonian which takes the form:

$$\begin{aligned} \langle \Psi_I^{\text{SM}} | H_{\text{BO}} + H_{\text{SOC}} + H_Z | \Psi_F^{S'M'} \rangle &= \delta_{\text{IF}} \delta_{\text{SS'}} \delta_{\text{MM'}} E_I^S \\ &+ \langle \Psi_I^{\text{SM}} | H_{\text{SOC}} + H_Z | \Psi_F^{S'M'} \rangle \end{aligned} \quad (8)$$

In this approach, the SOC operator is approximated by the spin-orbit mean field (SOMF) operator,³⁸ which is an effective one-electron operator that contains one- and two-electron SOC integrals and also incorporates the spin-other orbit interaction. Hence in eqn (8) H_{SOC} is given by

$$H_{\text{SOC}} = \sum_i h^{\text{SOC}}(x_i) s(i) \quad (9)$$

where $h^{\text{SOC}}(x_i)$ is the effective mean-field one-electron spin-orbit operator, and x_i and $s(i)$ refer to the coordinates and spin-operators of electron i , respectively.

2.2 Quantum dynamics simulations

The time-dependent (TD) Schrödinger equation within the diabatic Hamiltonian approach is solved by means of the multi-configuration time-dependent Hartree (MCTDH) method³⁹ where the TD wavefunction is expressed as a linear combination of Hartree products, so-called single particle functions (SPFs). The SPFs are represented by multi-set formulation⁴⁰ to adopt the present non-adiabatic correction problem. Here the primitive basis sets are chosen as harmonic oscillators' wavefunction in discrete variable representation (DVR). The initial wavefunction is taken as the product of harmonic wavefunctions at their vibrational ground state of the S_0 electronic ground state. The simulation of the absorption is based on the initial population of S_3 allowed electronic transition at time zero. The calculations have been performed with the Heidelberg MCTDH package version 8.4.13.⁴¹

2.3 Vibronic and spin-orbit couplings

Vibronic coupling theory has been developed in connection with a model Hamiltonian based on a diabatic representation of the electronic states.⁴² The diabatic Hamiltonian describing η_{el} coupled electronic states is written as

$$H(Q) = (T_N + V_0(Q))\Pi + W(Q) \quad (10)$$



where T_N is the kinetic energy operator, $V_0(Q)$ is the potential energy of some reference electronic state, usually the electronic ground state, Π is the $\eta_{\text{el}} \times \eta_{\text{el}}$ identity matrix and $W(Q)$ is the coupling matrix that contains the electronic eigenvalues, the $\kappa_i^{(n)}$ intrastate and the $\lambda_i^{(n,m)}$ inter-state vibronic couplings for n and m electronic states and i nuclear degree of freedom. The theory has been extended in order to include spin-orbit couplings in the formalism⁴³ within the spin-vibronic concept.⁴⁴

The intrastate $\kappa_i^{(n)}$ and inter-state linear $\lambda_i^{(n,m)}$ vibronic coupling constants generated by the vibrational molecular activity regulated by molecular symmetry rules are obtained by analytical formula when only two electronic states are involved within the linear vibronic coupling model.⁴⁰ The coupling constants can be deduced from electronic structure calculations using the first and second derivatives of the adiabatic potential energy surfaces $V_n(Q)$ with respect to Q_i at the ground state equilibrium geometry. Alternatively, and in order to go beyond the pair of states approximation and the linear formalism, $\lambda_i^{(n,m)}$ can be computed on the basis of the overlap matrix between the electronic wavefunctions at close-lying geometries⁴⁵ as an adiabatic-to-diabatic transformation matrix, such that the linear vibronic coupling (LVC) constants can be obtained by means of numerical differentiation.

$$\lambda_i^{(n,m)} = \frac{\partial}{\partial Q_i} \langle \Phi_n | H_{\text{el}} | \Phi_m \rangle \Big|_0 \quad (11)$$

where H_{el} is the electronic Hamiltonian and Φ are the diabatic wavefunctions.

The method is applicable to wavefunction-based methods as well as to TD-DFT, as used in the present study. In the latter case the wavefunctions are replaced by auxiliary many-electron wavefunctions.⁴⁶ The theory and construction of the $W(Q)$ coupling matrix, SOC, intra- and inter-state vibronic couplings are detailed in the ESI.† The S_n and T_n notation is kept all along the manuscript. This is justified by the use of a model Hamiltonian based on a diabatic representation of the electronic states, both singlet and triplet. Of course, “spin-orbit” states could be retrieved by diagonalization of the $W(Q)$ coupling matrix.

3 Results and discussion

The calculations reported in the next sections have been performed using the ADF quantum chemistry software.⁴⁷

3.1 Absorption spectra, structural and electronic properties of $[\text{Pt}(\text{pCp})(\text{acac})] \mathbf{1}$ and $[\text{Pt}(\text{pCpz})(\text{acac})] \mathbf{2}$

Both complexes adopt the common square-planar geometry associated with Pt(II) 5d⁸ electronic configuration and closed shell singlet ground state (Fig. 1). The structures of **1** and **2** are very close (Table S1, ESI†). The Pt–C distances are almost identical, 2.010 and 2.020 Å for **1** and **2** and so are the Pt–N distances, 2.008 and 1.982 Å, respectively (Fig. S1, ESI†). We observe a *trans* effect, the Pt–O distance *trans* to the carbon atom is roughly 0.1 Å longer than the one *trans* to the nitrogen atom, 2.129 and 2.035 Å, respectively, in **1**. It should be mentioned that only one conformation of the paracyclophane is stable. The upper ring of the paracyclophane comes close to

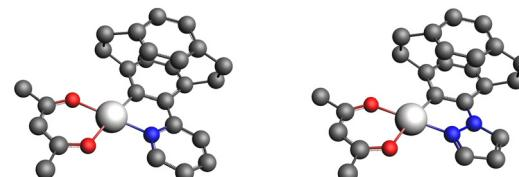


Fig. 1 Optimized geometries of the enantiomer A of **1** (left) and **2** (right). Hydrogen atoms have been omitted for the sake of clarity.

the metal cation leading to a C–C–C–C dihedral angle of 57.8° in **1**. No structures were found with an angle higher than 90°, with the upper ring going the opposite of the metal cation: all attempts led back to the original structure.

The structures of the enantiomers A and B, together with the frontier Kohn–Sham orbitals, are depicted in Fig. S2 and S3 (ESI†).

The absorption spectra were computed on the optimized structures of **1** and **2** and are represented in Fig. 2. Transition energies to the low-lying singlet excited states and associated oscillator strengths are reported in Table 1.

The analysis of the electronic character of the low-lying singlet and triplet excited states calculated at FC is provided in Fig. 3a (complex **1**) and 3b (complex **2**).

The absorption band of **1** starts at 411 nm (S_1) with an electronic transition mainly centered on the pyridine ligand py of LC_{Py} nature with a minor contribution of platinum-to-pyridine charge transfer so-called MLCT_{Py} (Fig. 3a). The second absorbing band is the convolution of S_2 and S_3 . The nature of S_2 is similar to that of S_1 . S_3 has a larger MLCT_{Py} contribution and even significant pyridine-to-acac charge transfer (LLCT_{acac}). This band is centered at 361 nm. Similarly to the singlet states, the triplet T_1 (471 nm) and T_2 (432 nm) are mainly LC_{Py} states. T_3 is completely different, mainly acac localized (Fig. 3a).

The absorption spectrum of **2** is significantly shifted towards higher energies compared to **1** in agreement with the experimental data.³⁵ The first band is generated by S_1 (349 nm) and S_2 (343 nm) which exhibit different natures. S_1 is mainly localized on the acceptor pyrazole ligand pz with an LC_{pz} character

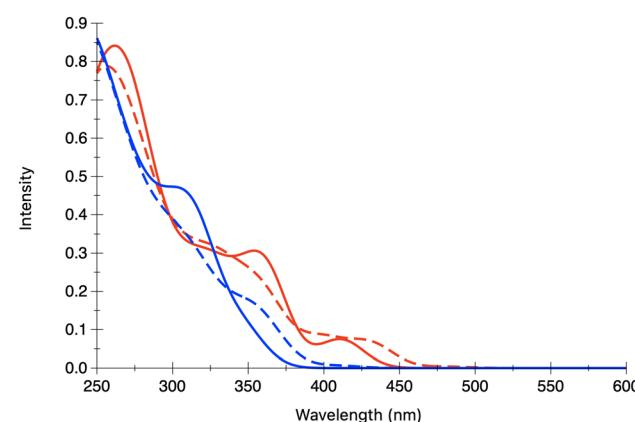


Fig. 2 Calculated TD-DFT absorption spectra of **1** (red trace) and **2** (blue trace) without (plain trace) and with (dashed trace) SOC.

Table 1 Transition energies E (in eV), oscillator strengths f and absorption wavelengths λ_{abs} (in nm) associated with the low-lying singlet and triplet excited states of **1** and **2**

Complex 1					
State	E (eV)	f	λ_{abs} (nm)	State	E (eV)
S_1	3.02	7.4×10^{-2}	411	T_1	2.63
S_2	3.42	7.7×10^{-2}	362	T_2	2.87
S_3	3.43	1.5×10^{-1}	361	T_3	3.09
S_4	3.53	2.7×10^{-2}	352	T_4	3.27
S_5	3.64	8.0×10^{-2}	340	T_5	3.36
S_6	3.77	2.3×10^{-2}	329	T_6	3.46
S_7	3.82	1.3×10^{-1}	324	T_7	3.53
S_8	3.91	5.8×10^{-3}	317	T_8	3.59
S_9	3.99	9.5×10^{-2}	311	T_9	3.64
S_{10}	4.09	2.7×10^{-3}	303	T_{10}	3.73
S_{11}	4.16	2.4×10^{-2}	298	T_{11}	3.85
S_{12}	4.17	4.2×10^{-3}	297	T_{12}	3.88
S_{13}	4.23	1.2×10^{-1}	293	T_{13}	3.94
S_{14}	4.25	2.8×10^{-4}	292	T_{14}	4.01
S_{15}	4.26	5.1×10^{-3}	291	T_{15}	4.04

Complex 2					
State	E (eV)	f	λ_{abs} (nm)	State	E (eV)
S_1	3.56	4.4×10^{-2}	349	T_1	3.08
S_2	3.61	5.6×10^{-2}	343	T_2	3.10
S_3	3.89	1.8×10^{-1}	319	T_3	3.36
S_4	3.95	4.8×10^{-2}	314	T_4	3.53
S_5	3.99	3.8×10^{-2}	311	T_5	3.59
S_6	4.06	1.0×10^{-1}	306	T_6	3.65
S_7	4.12	1.3×10^{-2}	301	T_7	3.75
S_8	4.19	6.7×10^{-2}	296	T_8	3.84
S_9	4.22	7.5×10^{-3}	294	T_9	3.93
S_{10}	4.29	1.1×10^{-1}	289	T_{10}	3.94
S_{11}	4.41	4.4×10^{-2}	281	T_{11}	3.98
S_{12}	4.48	4.8×10^{-2}	277	T_{12}	4.00
S_{13}	4.52	2.6×10^{-2}	274	T_{13}	4.11
S_{14}	4.57	4.6×10^{-2}	272	T_{14}	4.13
S_{15}	4.61	1.6×10^{-2}	269	T_{15}	4.18

(Fig. 3b), whereas S_2 has a mixed LLCT_{acac}/MLCT_{acac} character with charge transfer towards the acac. The intense absorption band at 319 nm is assigned to S_3 which has a very mixed nature. As far as the lowest triplet states are concerned, their nature is significantly different from those of **1**. For complex **2**, the pyrazole contribution is strongly reduced in T_1 and T_2 which are characterized by an increasing LC_{acac} contribution (Fig. 3b).

Such differences in the state character of **1** and **2** can easily be explained by the difference of frontier orbitals (Fig. S2 and S3, ESI[†]). For both complexes, the HOMO is delocalized over the platinum cation and the phenyl ring. Its energy is almost unaffected when substituting the pyridyl moiety (-5.624 eV) by a pyrazole moiety (-5.680 eV). In contrast, in **1**, the LUMO and LUMO+1 are almost purely localized on the pyridyl ligand and the acac ligand with significant energy differences, -1.927 and -1.445 eV, respectively. For **2**, their nature is mixed, half acac, and half pyrazole and the LUMO (-1.462 eV) and LUMO+1 (-1.377) are much closer in energy. The shift of the absorption spectra of **2** towards higher energy is attributed to the destabilization of the paracyclophane LUMO.

For both complexes, the inclusion of SOC significantly modifies the absorption spectra with a red-shift of the absorption of tens of nanometers. For **1**, the absorption with SOC starts at 483 nm with E_1 , E_2 and E_3 (Table 2) which are purely

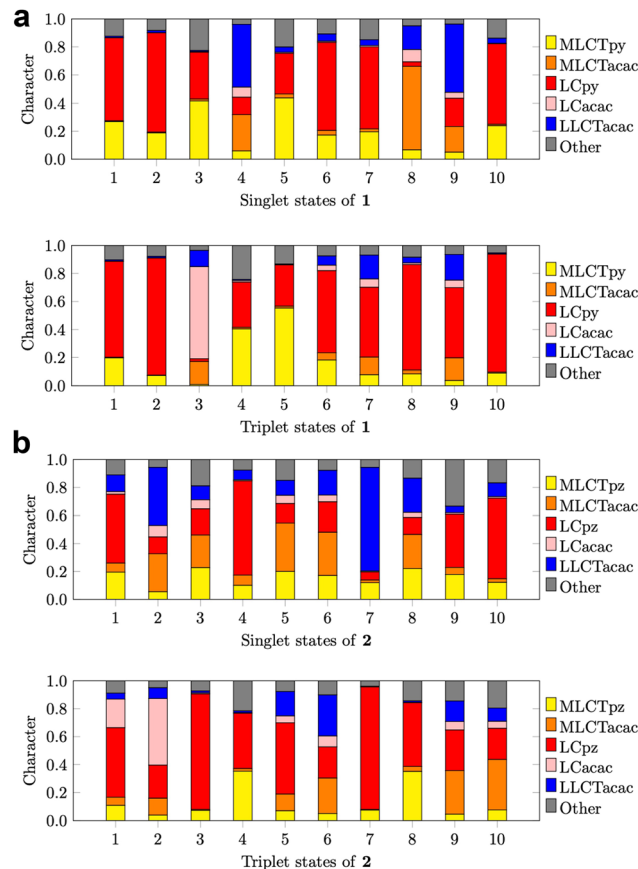


Fig. 3 (a) Electronic character of the 10 low-lying singlet and triplet excited states of complex **1** at FC from TheoDore analysis⁴⁸ (Ligand for pyridine so-called py). (b) Electronic character of the low-lying singlet and triplet excited states of complex **2** at FC from TheoDore analysis.⁴⁸ (Ligand for pyrazole so-called pz).

issued from T_1 . They are followed by a second set, E_4 , E_5 and E_6 , between 439 and 437 nm almost purely generated from T_2 . A first intense band at 429 nm (E_7), composed of S_1 / T_2 , T_4 and T_5 mixing, corresponds to the experimental one observed at 434 nm.³⁵ A second band is due to the convolution of E_{13} at 400 nm and E_{14} at 396 nm. E_{13} is mainly issued from T_4 with small contributions of S_2 , S_3 and S_5 . E_{14} is mainly a combination of S_3 and T_5 . These transitions correspond to the experimental absorption centered around 380 nm.

The effect of SOC on the spectra of **2** is somehow different. The destabilization of the LUMO and the energetic proximity of the LUMO+1 lead to a significant mixing between T_1 and T_2 at FC geometry, resulting in E_1 to E_6 states (Table 2). In contrast to **1**, for **2** the next set of states (E_7 to E_{12}) is composed of a mixture of T_3 and T_4 . The first states with significant singlet contribution are E_{13} (361 nm) and E_{14} (359 nm), generated by the mixing of S_1 and S_2 along with T_4 , T_5 and T_6 contributions. This band is in good agreement with the experimental first absorption peak located at 370 nm.³⁵

The overall computed absorption spectra of complexes **1** and **2** reproduce the maxima observed experimentally (Table S1, ESI[†]).³⁵



Table 2 Transition energies E (in eV), wavelengths λ_{abs} (in nm) and oscillator strengths F associated with the low-lying “spin-orbit” excited states of complexes **1** and **2** at FC geometry

Complex 1			
E (eV)	λ_{abs} (nm)	F	Composition
E ₁	2.569	483	1.3 × 10 ⁻⁴ 93% T1
E ₂	2.570	482	3.7 × 10 ⁻⁴ 93% T1
E ₃	2.573	482	3.4 × 10 ⁻³ 93% T1
E ₄	2.823	439	5.7 × 10 ⁻³ 80% T2 7% S1
E ₅	2.828	438	4.4 × 10 ⁻⁵ 84% T2 6% T4 6% T5
E ₆	2.835	437	7.9 × 10 ⁻³ 84% T2
E ₇	2.893	429	5.2 × 10 ⁻² 69% S1 10% T5 8% T2 6% T4
E ₈	3.044	407	3.5 × 10 ⁻⁴ 86% T3
E ₉	3.045	407	7.6 × 10 ⁻⁴ 86% T3
E ₁₀	3.046	407	1.2 × 10 ⁻³ 86% T3

Complex 2			
E_a (eV)	λ_{abs} (nm)	F	Composition
E ₁	3.022	410	3.4 × 10 ⁻⁴ 82% T1 9% T2
E ₂	3.023	410	3.1 × 10 ⁻⁴ 83% T1 9% T2
E ₃	3.026	410	3.5 × 10 ⁻³ 94% T1
E ₄	3.053	406	1.1 × 10 ⁻⁴ 84% T2 9% T1
E ₅	3.054	406	1.1 × 10 ⁻³ 84% T2 10% T1
E ₆	3.055	406	1.0 × 10 ⁻³ 94% T2
E ₇	3.311	374	2.3 × 10 ⁻³ 57% T3 25% T4
E ₈	3.316	374	3.1 × 10 ⁻⁴ 65% T3 21% T4
E ₉	3.326	373	3.4 × 10 ⁻³ 72% T3 16% T4
E ₁₀	3.362	369	4.2 × 10 ⁻³ 42% T4 35% T3 7% S1

After optimization of the lowest triplet states of **1** and **2**, two minima, the electronic density of which are reported in Fig. 4, were identified on the lowest triplet potential energy surface (PES). The first one, T_{1a} , is generated by the former T_1 state at Franck-Condon geometry and remains mainly localized on the pyridine and pyrazole ligands.

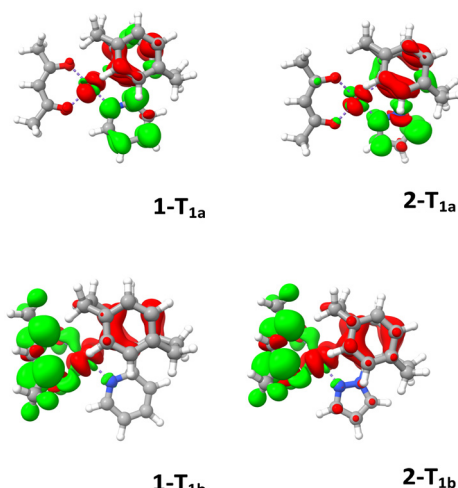


Fig. 4 Differences in electronic densities between the electronic ground state and the triplet states **1-T_{1a}** and **1-T_{1b}** (complex **1**) and **2-T_{1a}** and **2-T_{1b}** (complex **2**) at their optimized structures (red: loss of electronic density; green: gain of electronic density).

Table 3 Energetics (in eV) of the low-lying T_{1a} and T_{1b} excited states of **1** and **2**, together with the potentially thermally activated triplet metal-centered (MC) states MC**1** and MC**2**. (The definition of E_{dist} , E_{em} , and E_{stab} is given in Scheme S2, ESI)

	Complex 1				Complex 2			
	T_{1a}	T_{1b}	MC1	MC2	T_{1a}	T_{1b}	MC1	MC2
E_{dist}	0.281	0.653	2.198	1.350	0.496	0.609	2.238	1.436
E_{em}	2.084	2.016	0.175	1.429	2.192	2.095	0.166	1.336
E_{stab}	2.365	2.669	2.373	2.779	2.687	2.704	2.404	2.772
λ_{em}	595	615	7098	867	566	592	7473	928

The associated geometry is weakly affected as compared to the FC structure. The most significant changes are the slipping of the two aryl rings of the paracyclophane measured by the CCCC dihedral angle which increases from 57.8° in S_0 to 63° in T_{1a} for **1**. The change is more drastic in **2** with an increase from 59.4° in S_0 to 73.1 in T_{1a} . In both complexes, there is also a contraction of the Pt–C distance by 0.050 Å.

The second minima identified in the triplet PES, T_{1b} , is generated by the acac ligand centered LC_{acac}, namely T_3 of **1** and T_2 of **2** (Fig. 3a and b). For both complexes, the Pt–O distance associated with the oxygen atom *trans* to the carbon atom decreases by 0.060 Å. However, the main modification is the out of plane distortion of the acac ligand.

For complex **1**, the two minima are well separated and the T_{1a} state is much more stable than the T_{1b} state (Table 3). In complex **2**, the T_{1a} state, strongly destabilized, is almost degenerate with T_{1b} (Table 3). In **2**, the two states are probably in competition for the emission. Both complexes possess low-lying metal-centered (MC) triplet states, over-stabilized as compared to the emissive states by out-of-plane distortion towards a nearly tetrahedral structure, and potentially thermally activated at 298 K (Fig. S4, ESI†).

On the basis of the electronic data reported above, we can clearly assign the strong emission observed in complex **1** at 583 nm to T_{1a} (Table 3) of LC_{py} character. In contrast, the attribution of the emission observed in complex **2** at 468 nm is more challenging.

3.2 Emission properties of $[\text{Pt}(\text{pCpy})(\text{acac})]$ **1** and $[\text{Pt}(\text{pCpz})(\text{acac})]$ **2**

In order to get a further understanding of the emissive properties of the two complexes we computed their phosphorescence and tentatively CPL spectra taking into account SOC and vibronic effects as described in the methodological approach (Section 2.1) and developed using the ORCA quantum chemistry software.²⁹

The experimental spectra of both complexes **1** and **2** exhibit strong emission at 583 and 468 nm, respectively (Fig. 5).³⁵

As expected from the electronic properties of the lowest triplet excited states, reported in the previous section, the emission spectrum of complex **1** reveals a well-structured band at 77 K indicating the major role of T_1 in the emission. In addition, T_1 is well separated from T_2 by 0.24 eV (Table 1) justifying the neglect of T_2 in the simulation of the phosphorescence spectrum by keeping only the three lowest spin-orbit



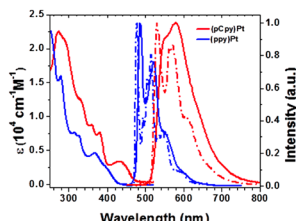


Fig. 5 Experimental absorption and emission spectra of **1** (left side and red trace) and **2** (right side and red trace) in CH_2Cl_2 and 2-Me-THF, respectively, at room temperature (solid line) and at 77 K (dashed line) (adapted from ref. 35 with permission of Elsevier).

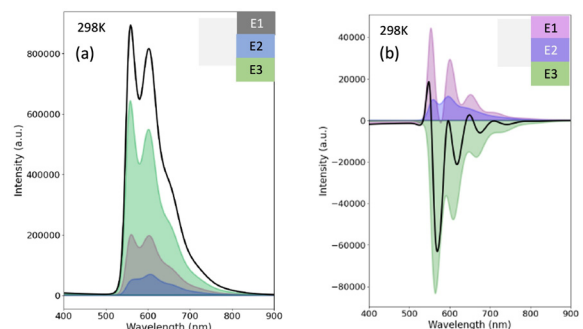
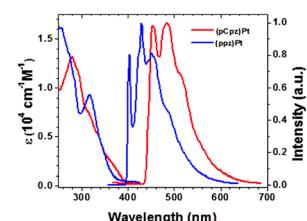


Fig. 6 Complex **1** calculated phosphorescence (a) and CPL (b) spectra of enantiomer A, at room temperature and phosphorescence spectrum at 77 K (c).

sublevels E_1 , E_2 , and E_3 originating from T_1 (Table 2). This assumption is more questionable for complex **2** characterized by nearly degenerate T_1 and T_2 states calculated at 3.08 and 3.10 eV, respectively (Table 1) leading to six nearly degenerate SO sublevels within 0.035 eV with mixed T_1/T_2 composition (Table 2). However, the computation of the Hessian in this tough case is the limiting step of our computational strategy. Consequently, the same computational strategy has been applied to both complexes.

Electronic ground states and first triplet excited states T_{1a} of **1** and **2** were fully optimized and their vibrational frequencies and Hessians calculated. Excited state dynamics (ESD) calculations of phosphorescence and CPL spectra were performed on all three first SOC states using ground state optimized structure and both ground state and T_1 Hessians. All three resulting phosphorescence spectra were weighted by Boltzmann distribution using ESD calculation's SOC states energies. Dissymmetry factors (g_{lum}) were calculated based on eqn (7) for SOC states calculated at T_1 optimized structure. Global g_{lum} was obtained from the addition of the three first SOC states g_{lum} weighted by Boltzmann distribution.

Calculated phosphorescence and CPL spectra of **1** at room temperature together with the most important spin-orbit sublevel contributions to their intensity are presented in Fig. 6. Deconvolution of the relevant spin-orbit sublevels in terms of M_s contributions, partial and total associated Boltzmann average radiative rate constants together with the partial and total relaxation times are given in Table 4.

The non-radiative relaxation has been neglected which is justified at low temperature (77 K). However, at room temperature not only intra-molecular processes such as internal conversion (IC) and intersystem crossing (ISC), but also external effects (environment, structural distortions, conformers, *etc.*) may induce non-radiative decay. This is illustrated experimentally in the case of complex **1** when comparing the well structured spectrum at 77 K and the broad band observed at room temperature (Fig. 5, left). The experimental value of the non-radiative constant which comprises both intramolecular and external effects occurring during the experiment, including the presence of low-lying metal-centred (MC) states, is evaluated at $1.5 \pm 0.1 \times 10^5 \text{ s}^{-1}$ for complex **1**.³⁵ This rather high value has to be compared to the calculated one, namely less than $0.009 \times 10^5 \text{ s}^{-1}$ obtained by the computational strategy developed in our

original work³⁰ that includes only the intramolecular effects within the harmonic approximation following the so-called weak-coupling limit of the energy gap law.⁴⁹ The weakness of the computational method, which is not complete enough to take into account the external effects, and the presence of potentially thermally activated MC states (Table 3) at 298 K make a direct comparison between the experimental and theoretical photophysical data tentative.

The simulated phosphorescence spectrum of complex **1** reproduces perfectly the shape of the experimental spectrum, especially at 77 K (Fig. 5 and 6), whereas the structure of the computed phosphorescence spectrum of complex **2**, based on the T_{1a} SO sublevels only, is poorly resolved (Fig. S5, ESI†). This confirms the weakness of our model when several nearly degenerate low-lying triplet states contribute to the emission spectroscopy.

For this reason, only the CPL spectrum of complex **1** has been calculated (Fig. 6, top, right side).

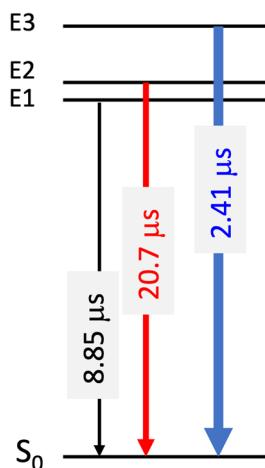
Deconvolution of the spectrum reveals that the emission process in complex **1** involves magnetic sublevels E_1 to E_3 (Scheme 2) with a major contribution of the E_3 state due to its rather large $M_s = 0$ component (>60%) (Table 4).

Despite a modest zero-field splitting (<15 cm^{-1}) the phosphorescence at room temperature is dominated by the fast $E_3 \rightarrow S_0$ emission process which provides the fastest relaxation (2.41 μs) through the rather large $M_s = 0$ contribution (>60%). At 77 K the $E_1 \rightarrow S_0$ decay is improved at the expense of $E_3 \rightarrow S_0$ leading to an increase in total relaxation time from 5.3 μs to 6.6 μs (Table 4) in agreement with the experimental trends. The estimated total relaxation time at 298 K agrees perfectly with



Table 4 Deconvolution of the relevant spin–orbit sublevels in terms of M_s contributions, partial k_r^n and total k_r associated Boltzmann average radiative rate constants together with the partial $\tau_{298,77K}^n$ and total $\tau_{298,77K}$ relaxation times and quantum yield ϕ calculated for complex **1**. Available experimental data are given for comparison

Complex 1	$M_s = 0$ (%)	$M_s = -1$ (%)	$M_s = +1$ (%)	Energy (cm ⁻¹)	k_r^n (10 ⁵ s ⁻¹)	τ_{298K}^n (μs)	k_r (10 ⁵ s ⁻¹)	τ_{298K} (μs)	τ_{77K} (μs)	ϕ
State										
E ₁	2.9	47.6	47.6	16 498	1.13	8.85				
E ₂	32.8	32.6	32.6	16 504	0.484	20.70				
E ₃	62.4	17.9	17.9	16 513	4.15	2.41				
Theory							1.88	5.3	6.6	0.32
Exp. ³⁵							0.37 ± 0.02	5.3	16.1	0.20



Scheme 2 Magnetic sublevel contributions and associated computed relaxation times from the relevant magnetic sublevels describing the phosphorescence of complex **1** at room temperature.

the experimental value which is fortuitous because the non-radiative corrections are neglected.

The CPL intensity is mainly governed by the magnitude and the relative orientations (angle θ , Table 5) of the electric and magnetic transition dipole moments and by the SOC interactions.³⁰ The calculated transition electric and magnetic dipole moments attributed to each SO sublevel E₁, E₂ and E₃ of complex **1**, enantiomer A, are reported in Table S1, ESI.[†] As expected, the flux of electronic density from the pyridine ligand to the metal/pyridine ligand that characterizes the T_{1a} → S₀ emissive process (Scheme 3) controls the magnitude and orientation of the dipoles, together with the induced magnetic anisotropy. The emission process *via* E₃ (62% $M_s = 0$) involves a mainly *z*-polarized magnetic dipole and *xy*-plane polarized electric dipole forming an angle of 57.6°. This results in a right circularly polarized emission characterized by a negative CPL signal of high intensity (Fig. 6, top right). The sub-level E₁, with negligible

$M_s = 0$ component and 47.6% $M_s = \pm 1$, entangles *xz*-plane polarized electric dipole and negligible magnetic dipole. The major contribution to $|g_{lum}|$ comes from E₂ equally composed of 33% of $M_s = 0$, $M_s = \pm 1$, with the formation of an optimum angle $\theta = 30.3^\circ$ resulting in an *x*-polarized magnetic dipole correlated to an *xy*-plane polarized electric dipole. Both E₁ and E₂ emissions are characterized by modest positive CPL intensities. Consequently, by cancellation, the differential CPL spectrum of complex **1** enantiomer A has modest negative intensity and $|g_{lum}| = 6.1 \times 10^{-3}$. The contribution of the metal-ligand charge transfer to the process is less favorable to the CPL activity than a pure intra-ligand charge transfer as demonstrated for π -conjugated helicenic Re(i) complexes.³⁰

3.3 Ultrafast decay (<1 ps) in complexes [Pt(pCpy)(acac)] **1** and [Pt(pCpz)(acac)] **2**

In order to go beyond the static picture and to compare the ultrafast photophysics (fs-ps) of complexes **1** and **2**, non-adiabatic quantum dynamics simulations including spin-vibronic effects⁴³ have been performed. As illustrated for a number of transition metal complexes, the high density of states in a limited domain of energy, the degree of electronic mixing and the correlation between electronic densities and nuclear vibrations generate crucial electron–vibration (vibronic) intrastate and inter-state couplings that control, together with SOC, the population in time of the individual excited states in the sub-ps regime.^{50–52}

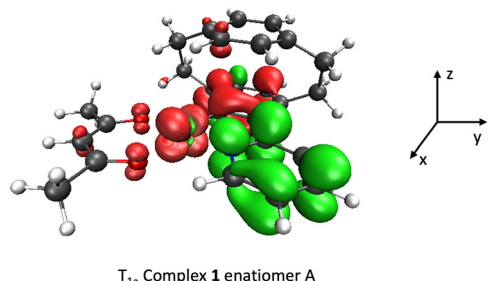
One important question related to the different electronic characters of the three low-lying triplet excited states of **1** and **2** is the interplay between T₁ and T₂, fully localized on the pyridine in **1** and delocalized over the pyrazol and the acac ligands in **2**, and the role of T₃, fully localized on the acac ligand in **1** and fully localized on the pyrazol in **2**, within the first ps. Clearly, the dialog between the nuclear vibrations and the electronic densities in play should lead to distinctive photo-physics. The process described here follows the time evolution of the diabatic population of the low-lying singlet and triplet excited states after initial vertical S₀ → S₃ absorption.

The electronic problem has been reduced to 3 singlet states (S₁, S₂, S₃) and 3 triplet states (T₁, T₂, T₃) leading to 12 “spin-orbit” states. The SOC terms introduced in the W(Q) coupling matrix (eqn (S14), ESI[†]) together with the intra- and inter-state couplings are reported in Tables S2–S4, ESI[†]. For both molecules, 20 active normal modes have been selected on the basis of significant intra-state $\kappa_i^{(n)}/\omega$ coupling amplitudes and large inter-state $\lambda_i^{(n,m)}$ coupling constants (Tables S3 and S4, ESI[†]).

Table 5 Calculated partial luminescence $|g_{lum}|$, associated θ angle in ° and spin–orbit sublevels energies for complex **1**

State	Energy (cm ⁻¹)	θ °	$ g_{lum} $
E ₁	16 498	59.4	0.00092
E ₂	16 504	30.3	0.01539
E ₃	16 513	57.6	0.00194
Boltzmann average $ g_{lum} $: 6.1×10^{-3}			





Scheme 3 The difference in electronic densities describing the $T_{1a} \rightarrow S_0$ emissive process in complex **1** enantiomer A (in green: loss of electronic density, in red: gain of density).

In addition, some normal modes have been selected on the basis of the number of one-Dim cuts of the PES crossings they generate (Fig. S6 and S7, ESI[†]). The 20 selected vibrational normal modes are depicted in Fig. S8 and S9 (ESI[†]).

The time evolution of the diabatic population of the low-lying singlet and triplet excited states of complexes **1** (left) and **2** (right) is shown in Fig. 7.

Within the constraints of our simulation (reduced nuclear and electronic dimensionalities, harmonic approximation) the ultrafast non-adiabatic dynamics of the pyridine and pyrazole-substituted complexes **1** and **2** differ drastically already within the first 150 fs, as far as the low-lying triplet states population is concerned. In complex **1** major inter-state S_3/S_1 and S_2/S_1 vibronic couplings activated by out-of-plane vibrations of the paracyclophane, acac and pyridine groups (Q_{129} , Q_{130} , Q_{132} , Fig. S8 and Table S4, ESI[†]) lead to a fast depopulation of S_3 at the benefit of S_1 and S_2 states within 20–30 fs. Simultaneously, large S_2/T_1 , S_3/T_1 and S_3/T_2 SOC induce an efficient population of T_1 and T_2 which exchange population with T_3 through vibronic effects driven by symmetric twisting of the acac and paracyclophane groups (Q_{128} , Fig. S8, ESI[†]). The transfer of population from S_1 to its nearly degenerate state T_3 and to T_2 is also favored by the PES crossings induced by these nuclear

vibrations (Q_{128} , Q_{129} , Q_{130}) in the range of 20–30 fs. The T_3 state localized on the acac ligand acts as a reservoir and plays a major role in the early time dynamics of complex **1**. At 150 fs the populations of S_1 and T_3 reach 20%, and that of S_3 decreased to 15%, with S_2 , T_1 and T_2 remaining marginally populated at ~10%. After 200 fs the population of S_1 decreases at the advantage of those of T_1 and T_2 by SOC and because of the number of S_1/T_2 crossings generated by the low frequency modes Q_{19} , Q_{20} , Q_{23} (Fig. S8, ESI[†]). The population of T_1 increases slowly by vibronic exchange with T_2 via these longer time-scale vibrations (acac and pyridine twisting, metal coordination sphere breathing) associated with these modes to approach 35% whereas the population of T_2 does not exceed 20% at 2 ps (Fig. S10, ESI[†]). At 2 ps T_1 and T_3 are nearly equally populated and we can predict that very low frequencies modes like out-of-plane distortion of the acac ligand, not relevant within the limit of our simulations, will stabilize T_1 as discussed above to converge to T_{1b} .

The low-lying electronic excited states of complex **1** are either mainly pyridine localized (S_1 , S_2 , T_1 , T_2) or acac localized (T_3), the absorbing state S_3 being mainly MLCT_{py} in nature. S_1 and S_2 are contaminated by MLCT_{py} contributions (Fig. 3a).

In contrast, the low-lying electronic excited states of complex **2** are largely mixed with minor MLCT contributions, the only rather pure state being T_3 localized on the pyrazole. Importantly, there is no pure LC_{acac} state (T_3 of complex **1**) the acac and pyrazole localized electronic densities being mixed in T_1 and T_2 . These differences in electronic character have important consequences for both SOC and vibronic couplings (Tables S2–S4, ESI[†]) and for the quantum dynamics spin-vibronic mechanism (Scheme 4). In particular, SO effects are less important in complex **2** and the ultrafast population (<30 fs) of the triplet states as observed in complex **1** does not occur. At 200 fs the three lowest triplet states T_1 , T_2 and T_3 remain marginally populated (<15%). The high frequency nuclear vibrations associated with normal modes Q_{125} and Q_{126} corresponding to the symmetric and asymmetric twisting of the acac and paracyclophane groups and Q_{124} and Q_{128} linked to the acac and paracyclophane groups induce large S_1/S_2 interstate vibronic coupling but modest S_1/S_3 coupling (Table S4, ESI[†]). Consequently, the depopulation of the S_3 absorbing state in complex **2** is rather slow as compared to

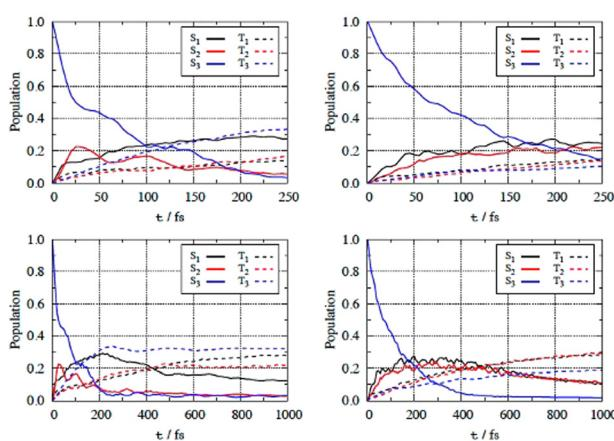
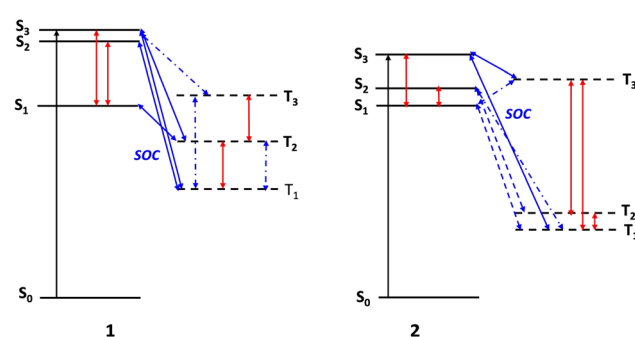


Fig. 7 Time-evolution of the diabatic populations of the low-lying excited states of complexes **1** (left) and **2** (right) within 250 fs (top) and 1 ps (bottom). The diabatic population for the T_n states represents the sum over the three SO sublevels.



Scheme 4 Spin-vibronic mechanism of ultrafast non-adiabatic dynamics within the low-lying singlet and triplet excited states of complex **1** (left) and complex **2** (right). (Blue trace: solid line for large SOC, dashed line for moderate SOC; red trace: vibronic coupling).



complex **1** (40% *vs.* 20% at 100 fs). These high frequency modes Q₁₂₅, Q₁₂₆, and Q₁₂₈ generate a number of PES crossings between S₁, S₂ and T₃ and between T₃, T₁ and T₂ (Fig. S7, ESI†) but the transfer of population to T₁ and T₂ remains moderate within the first 200 fs.

Finally, strong interstate vibronic couplings between T₁ and T₂, the two nearly degenerate triplet states localized equally on the acac and pyrazole ligands and induced by a dozen of both high- and low-frequency normal modes in complex **2** (Table S4, ESI†) confirm our hypothesis developed within the context of the emission, namely the participation of both triplet states in the phosphorescence and CPL activity. The simulation of realistic phosphorescence and CPL spectra in this case is out of reach with the current methodological developments.

4 Conclusion

The spin-orbit effects hidden behind the photophysics of phosphorescent chiral cyclometalated Pt(II) complexes namely [Pt(pCpy)(acac)] **1** and [Pt(pCpz)(acac)] **2** have been deciphered by combining different methods of quantum chemistry based on density functional theory and non-adiabatic quantum dynamics, including spin-orbit and vibronic effects. This theoretical study has enabled us to simulate absorption and phosphorescence spectra for complexes **1** and **2** and CPL spectrum for complex **1** and to decrypt the relevant spin-orbit sublevels contributing to the radiative rate constants and phosphorescence relaxation times. Sub-picosecond non-adiabatic quantum dynamics suggest a spin-vibronic mechanism driven by paracyclophane and acac nuclear vibrations.

These two very similar molecules, differing by the aromatic ring, pyridine (**1**) or pyrazole (**2**) attached to the paracyclophane exhibit very different characteristics in various aspects:

(i) The computational difficulties, correlated to the complexity of the electronic and vibrational problems, make complex **1** an “easy case” and complex **2** a “tough case”.

(ii) The energetics and electronic densities of the low-lying triplet states involved in the emission properties.

(iii) The pyridine or acac ligand-localized electronic structure of the three lowest triplets in complex **1** *vs.* a delocalized electronic structure over the acac and pyrazole ligands in the two lowest nearly-degenerate triplet states in complex **2**.

(iv) The absorbing state has mixed LC_{py}/MLCT_{py} character in complex **1** whereas the absorbing state is significantly mixed with MLCT_{acac} and LLCT contributions in complex **2**;

(v) A well-resolved, intense and realistic phosphorescence spectrum has been obtained for complex **1** on the basis of the single lowest T₁ state, mainly localized on the pyridine with a small charge transfer from Pt(II), while this strategy provided a rather poor phosphorescence spectrum, not comparable to the experimental one for complex **2** which needs the inclusion of both T₁ and T₂ states delocalized over the pyrazole and acac ligands in the simulation.

The non-adiabatic quantum dynamics simulations show an ultrafast decay driven by both spin-orbit and vibronic

couplings in complex **1** with an efficient population of the acac localized triplet state within 150 fs. This ultrafast decay is driven by symmetric twisting and out-of-plane vibrations of the paracyclophane and acac groups and large SOC between the singlet and triplet manifolds. At 2 ps the diabatic population of T₁ reaches 35% whereas the one of T₂ does not exceed 20%. In contrast, the initial decay of the absorbing state in complex **2** is rather slow because of moderate spin-vibronic effects attributed to the delocalized electronic densities in play and the minor metal-ligand charge transfer contributions. The nearly degenerate T₁ and T₂ excited states remain strongly coupled by intrastate vibronic coupling activated by a number of normal modes of high and low frequencies. This confirms that in order to obtain correct phosphorescence and CPL spectra both T₁ and T₂ excited states have to be included in the simulation of the spectra of complex **2**, which is challenging at the level of theory used in the present work. Further theoretical developments should allow efficient calculation of the Hessian for several nearly degenerate electronic excited states and improve the computation of non-radiative constants including not only external effects but also the presence of thermally activated MC states.

The circularly polarized luminescence spectrum of complex **1**, enantiomer A, has been predicted on the basis of the magnitude and relative orientation of the transition electric and magnetic dipole moments calculated for each SO sublevel expressed in terms of M_s components. The CPL activity, characterized by a relatively modest calculated g_{lum} value (<10⁻²), is governed by the flux of electronic density from the pyridine to the metal/pyridine generated during the emission process. This flux controls the magnitude and orientation of the dipoles together with the induced magnetic anisotropy. The major contribution to g_{lum} comes from the SO sublevel equally composed of 33% of M_s = 0, M_s = ±1 with an optimum angle of ~30° between the electric and magnetic dipole moments. However, the intensity generated by this SO state is partially cancelled by the major contribution of the SO sublevel composed at 62% of the M_s = 0 component to the emission process, resulting in a negative CPL signal of high intensity generated by z-polarized magnetic and xy-plane polarized electric dipoles forming an angle of ~60°.

This comprehensive theoretical study paves the way for the synthesis of new chiral Pt(II) paracyclophane complexes with optimal electronic and structural properties. The new molecules should fulfill several criteria based on the energetics of the lowest triplet states and their SO sublevels: the T₁–T₂ energy gap has to be increased and the SO sublevels with dominant M_s = ±1 component should not be contaminated by M_s = 0 to warranty an efficient CPL activity. The acac ligand is clearly non-innocent. The substitution of the acac ligand and the nature of the aromatic ring linked to the paracyclophane may help in controlling the relative energetic and electronic composition of the ligand-centered states which play a key role here. However, metal-charge transfer contributions may be important in order to promote efficient decay to the triplet excited states or relevant spin-orbit coupling and splitting. As proposed experimentally, and confirmed by preliminary calculations, the presence of thermally activated MC states may be



responsible for partial quenching of phosphorescence. Bulky ligands may prevent their activation by inhibiting their stabilization *via* tetrahedral distortion.

Author contributions

T. G. and C. G. performed electronic structure calculations, analyzed the results and contributed equally to the writing of the manuscript. S. M. and C. D. performed the QD simulations and C. D. has been involved in the conceptualization, theoretical development and interpretation, analysis, methodology and writing.

Data availability

The data supporting this article have been included as part of the ESI.† The code for the description of the software can be found at <https://www.scm.com/amsterdam-modeling-suite/adf/> and <https://www.pci.uni-heidelberg.de/tc/mctdh.html>.

Conflicts of interest

There are no conflicts to declare.

Acknowledgements

T. G. acknowledges the ANR-21-CE29-0015 “ChirON” for funding support and the Molecular Theory and Spectroscopy group at the MPI, Mülheim, more particularly Dr Dimitrios Manganas for scientific discussions and initiation into ORCA. The authors acknowledge Dr Dimitrios Manganas and Prof Matteo Mauro for helpful discussions at the preliminary stage of the project and M. Guillaume Rouaut and M. Even Chiari for technical support. The calculations have been performed at the regional HPC, Strasbourg, through a grant of computer time.

References

- V. M. Miskowski, V. H. Houlding, C.-M. Che and Y. Wang, *Inorg. Chem.*, 1993, **32**, 2518–2524.
- J. A. G. Williams, *Top. Curr. Chem.*, 2007, **281**, 205–268.
- J. A. G. Williams, S. Develay, D. L. Rochester and L. Murphy, *Coord. Chem. Rev.*, 2008, **252**, 2596–2611.
- J. A. G. Williams, *Chem. Soc. Rev.*, 2009, **38**, 1783–1801.
- L. Murphy and J. A. G. Williams, *Top. Organomet. Chem.*, 2010, **28**, 75–111.
- J. E. Yarnell, I. Davydenko, P. V. Dorovatovskii, V. N. Khrustalev, T. V. Timofeeva, F. N. Castellano, S. R. Marder, C. Risko and S. Barlow, *J. Phys. Chem. C*, 2018, **122**, 13848–13862.
- A. Haque, L. Xu, R. A. Al-Balushi, M. K. Al-Suti, R. Ilmi, Z. Guo, M. S. Kahn, W.-Y. Wong and P. R. Raithby, *Chem. Soc. Rev.*, 2019, **48**, 5547–5563.
- Y. Han, Z. Gao, C. Wang, R. Zhong and F. Wang, *Coord. Chem. Rev.*, 2020, **414**, 213300.
- V. W.-W. Yam and A. S.-Y. Law, *Coord. Chem. Rev.*, 2020, **414**, 213298.
- M. A. Soto, R. Kandel and M. J. MacLachlan, *Eur. J. Inorg. Chem.*, 2021, 894–906.
- A. Haque, H. El Moll, K. M. Alenezi, M. S. Kahn and W.-Y. Wong, *Materials*, 2021, **14**, 4236.
- V. W.-W. Yam and Y.-H. Cheng, *Bull. Chem. Soc. Jpn.*, 2022, **95**, 846–854.
- Highly Efficient OLEDs with Phosphorescent Materials*, ed. H. Yersin, Wiley-VCH, Weinheim, 2008.
- D.-W. Zhang, M. Li and C.-F. Chen, *Chem. Soc. Rev.*, 2020, **49**, 1331–1343; J. Han, S. Guo, H. Lu, S. Liu, Q. Zhao and W. Huang, *Adv. Opt. Mater.*, 2018, **6**, 1800538.
- C. Wagenknecht, C.-M. Li, A. Reingruber, X.-H. Bao, A. Goebel, Y.-A. Chen, Q. Zhang, K. Chen and J.-W. Pan, *Nat. Photonics*, 2010, **4**, 549.
- R. Farshchi, M. Ramsteiner, J. Herfort, A. Tahraoui and H. T. Grahn, *Appl. Phys. Lett.*, 2011, **98**, 162508; J. R. Brandt, F. Salerno and M. J. Fuchter, *Nat. Rev. Chem.*, 2017, **1**, 45.
- T. Sajoto, P. I. Djurovich, A. B. Tamayo, J. Osgaard, W. A. Goddard III and M. E. Thompson, *J. Am. Chem. Soc.*, 2009, **131**, 9813–9822.
- C. Adachi, M. A. Baldo, M. E. Thompson and S. R. Forrest, *J. Appl. Phys.*, 2001, **90**, 5048.
- N. Saleh, C. Shen and J. Crassous, *Chem. Sci.*, 2014, **5**, 3680–3694.
- N. Hellou, M. Srebo-Hooper, L. Favreau, F. Zinna, E. Caytan, L. Toupet, V. Dorcet, M. Jean, N. Vanthuyne, J. A. G. Williams, L. Di Bari, J. Autschbach and J. Crassous, *Angew. Chem., Int. Ed.*, 2017, **56**, 8236–8239.
- N. Saleh, M. Srebo, T. Reynaldo, N. Vanthuyne, L. Toupet, V. Y. Chang, G. Muller, J. A. G. Williams, C. Roussel, J. Autschbach and J. Crassous, *Chem. Commun.*, 2015, **51**, 3754–3757.
- E. S. Gauthier, L. Abella, N. Hellou, B. Darqui, E. Caytan, T. Roisnel, N. Vanthuyne, L. Favreau, M. Srebo-Hooper, J. A. G. Williams, J. Autschbach and J. Crassous, *Angew. Chem., Int. Ed.*, 2020, **59**, 8394–8400.
- C. Shen, E. Anger, M. Srebo, N. Vanthuyne, K. K. Deol, T. D. Jefferson, G. Muller, J. A. G. Williams, L. Toupet, C. Roussel, J. Autschbach, R. Réau and J. Crassous, *Chem. Sci.*, 2014, **5**, 1915–1927.
- J. R. Brandt, X. Wang, Y. Yang, A. J. Campbell and M. J. Fuchter, *J. Am. Chem. Soc.*, 2016, **138**, 9743–9746.
- D. Kundu, D. Jelonek, N. Del Rio, N. Vanthuyne, M. Srebo-Hooper and J. Crassous, *Chem. – Asian J.*, 2025, e202401735.
- C. Gourlaouen and C. Daniel, *Dalton Trans.*, 2014, **43**, 17806–17819.
- J. Autschbach and T. Ziegler, *J. Chem. Phys.*, 2002, **116**, 891.
- (a) O. Vahtras, H. Agren, P. Jorgensen, J. J. A. Jensen, T. Helgaker and J. Olsen, *J. Chem. Phys.*, 1992, **97**, 9178; (b) F. Wang and T. Ziegler, *J. Chem. Phys.*, 2005, **123**, 154102.
- F. Neese, Software update: the ORCA program system – Version 5.0, *Wiley Interdiscip. Rev.: Comput. Mol. Sci.*, 2022, **12**(1), e1606, DOI: [10.1002/wcms.1606](https://doi.org/10.1002/wcms.1606).
- R. Shafei, A. Hamano, C. Gourlaouen, D. Manganas, K. Takano, C. Daniel and F. Neese, *J. Chem. Phys.*, 2023, **159**, 084102.
- S. E. Gibson and J. D. Knight, *Org. Biomol. Chem.*, 2033, **1**, 1256–1269.



32 A. Yanagawa, R. Inoue and Y. Morisaki, *Chem. Commun.*, 2024, **60**, 1468–1471.

33 J. J. P. Kramer, M. Nieger and S. Bräse, *Eur. J. Org. Chem.*, 2013, 541–549.

34 S. E. Gibson and J. D. Knight, *Org. Biomol. Chem.*, 2003, **1**, 1256–1269.

35 B. K. T. Batagoda, P. I. Djurovich, S. Bräse and M. E. Thompson, *Polyhedron*, 2016, **116**, 182–188.

36 N. O. Foglia, D. Manganas and F. Neese, *J. Chem. Phys.*, 2022, **157**, 154106; F. Neese and E. I. Solomon, *Inorg. Chem.*, 1999, **38**, 1847; D. Ganyushin and F. Neese, *J. Chem. Phys.*, 2008, **128**, 114117.

37 M. Atanasov, D. Aravena, E. Suturina, E. Bill, D. Manganas and F. Neese, *Coord. Chem. Rev.*, 2015, **289**, 177–214.

38 F. Neese, *J. Chem. Phys.*, 2005, **122**, 34107.

39 *Multidimensional Quantum Dynamics: MCTDH Theory and Applications*, ed. H.-D. Meyer, F. Gatti and G. A. Worth, Wiley-VCH, Weinheim, 2009.

40 U. Manthe, H.-D. Meyer and L. S. Cederbaum, *J. Chem. Phys.*, 1992, **97**, 9062–9071.

41 H.-D. Meyer, G. A. Worth, M. H. Beck, A. J.ckle, U. Manthe, M. Ehara, A. Raab, M.-C. Heitz, S. Sukiasyan, C. Cattarius, S. Wefing, F. Gatti, M. Nest, F. Otto, M. R. Brill, O. Vendrell, M. Schröder and D. Pelaez, *The MCTDH Package, Version 8.4*, see <https://mctdh.uni-hd.de/> (2007).

42 H. Köppel, W. Domcke and L. S. Cederbaum, *Adv. Chem. Phys.*, 1984, **57**, 59–246.

43 J. Eng, C. Gourlaouen, E. Gindensperger and C. Daniel, *Acc. Chem. Res.*, 2015, **48**, 809–817.

44 T. J. Penfold, E. Gindensperger, C. Daniel and C. M. Marian, *Chem. Rev.*, 2018, **118**, 6975–7625.

45 F. Plasser, M. Ruckenbauer, S. Mai, M. Oppel, P. Marquetand and L. Gonzalez, *J. Chem. Theory Comput.*, 2016, **12**, 1207–1219.

46 M. Fumanal, F. Plasser, S. Mai, C. Daniel and E. Gindensperger, *J. Chem. Phys.*, 2018, **148**, 124119.

47 ADF2019, SCM, Theoretical Chemistry, Vrije Universiteit, Amsterdam, The Netherlands: <https://www.scm.com>.

48 F. Plasser, *J. Chem. Phys.*, 2020, **152**, 084108.

49 R. Englman and J. Jortner, *Mol. Phys.*, 1970, **18**, 145–164.

50 C. Daniel, *Phys. Chem. Chem. Phys.*, 2021, **23**, 43–58.

51 S. Mandal and C. Daniel, *Phys. Chem. Chem. Phys.*, 2023, **25**, 18720–18727.

52 S. Mandal and C. Daniel, *J. Phys. Chem. A*, 2024, **128**(16), 3126–3136.

